Unbiased constraints on ultralight axion mass from dwarf spheroidal galaxies

Unbiased constraints on ultralight axion mass from dwarf spheroidal galaxies

Alma X. González-Morales[1,2]★, David J. E. Marsh[3], Jorge Peñarrubia[4],
L. Arturo Ureña-López[2]

[1] *Departamento de Física, DCI, Campus León, Universidad de Guanajuato, 37150, León, Guanajuato, México*
[2] *Consejo Nacional de Ciencia y Tecnología, Av. Insurgentes Sur 1582.*
Colonia Crédito Constructor, Del. Benito Jurez C.P. 03940, México D.F. México
[3] *Department of Physics, King's College London, Strand, London, WC2R 2LS, UK*
[4] *Institute for Astronomy, University of Edinburgh, Royal Observatory, Blackford Hill, Edinburgh EH9 3HJ, UK*

22 August 2017

ABSTRACT
It has been suggested that the internal dynamics of dwarf spheroidal galaxies (dSphs) can be used to test whether or not ultralight axions with $m_a \sim 10^{-22}$ eV are a preferred dark matter candidate. However, comparisons to theoretical predictions tend to be inconclusive for the simple reason that while most cosmological models consider only dark matter, one observes only baryons. Here we use realistic kinematic mock data catalogs of Milky Way dSph's to show that the "mass-anisotropy degeneracy" in the Jeans equations leads to biased bounds on the axion mass in galaxies with unknown dark matter halo profiles. In galaxies with multiple chemodynamical components this bias can be partly removed by modelling the mass enclosed within each subpopulation. However, analysis of the mock data reveals that the least-biased constraints on the axion mass result from fitting the luminosity-averaged velocity dispersion of the individual chemodynamical components directly. Applying our analysis to two dSph's with reported stellar subcomponents, Fornax and Sculptor, and assuming that the halo profile has not been acted on by baryons, yields core radii $r_c > 1.5$ kpc and $r_c > 1.2$ kpc respectively, and $m_a < 0.4 \times 10^{-22}$ eV at 97.5% confidence. These bounds are in tension with the number of observed satellites derived from simple (but conservative) estimates of the subhalo mass function in Milky Way-like galaxies. We discuss how baryonic feedback might affect our results, and the impact of such a small axion mass on the growth of structures in the Universe.

Key words: gravitation, galaxies: Local Group, galaxies: dwarf, cosmology: dark matter

1 INTRODUCTION

axion dark matter is described by a classical scalar field, and differs from Cold Dark Matter (CDM, which is described by collisionless particles) on scales below the de Broglie wavelength due to the presence of gradient energy (see Hui et al. 2017; Marsh 2016; Suárez et al. 2014, for a review). For ultralight axions (ULAs) with $m_a/10^{-22}$ eV $\equiv m_{22} \approx 1$ this scale is large enough to be of relevance for the cusp-core problem in dSphs, as well as alleviating various other small scale issues with CDM (Hu et al. 2000; Marsh & Silk 2014; Schive et al. 2014a; Matos & Urena-Lopez 2001, 2000; Sahni

& Wang 2000; Hu et al. 2000).[1] On non-linear scales, axion DM forms a class of pseudo-soliton known as an oscillaton, or "axion star" (Ruffini & Bonazzola 1969; Seidel & Suen 1991; Urena-Lopez 2002; Guzman & Urena-Lopez 2004). The soliton is supported against gravitational collapse by gradient energy, and is expected to form in the centres of ULA halos. On larger scales, since structure formation proceeds just as for CDM, ULA halos should resemble the NFW profile (Navarro et al. 1997). Indeed, the NFW profile is

★ E-mail: alma.gonzalez@fisica.ugto.mx

---

[1] Note that a mass scale of order of 10^{-22}eV has for a long time been a recurring result in the studies of axion or scalar field models for galaxy halos and small scale structure, see for instance(Press et al. 1990; Sin 1994; Sahni & Wang 2000; Arbey et al. 2001; Matos & Urena-Lopez 2001; Hu et al. 2000).

found from collisionless N-body simulations, which are operationally equivalent to the axion model on scales above the de Broglie wavelength (e.g. Widrow & Kaiser 1993; Uhlemann et al. 2014). High-resolution cosmological simulations and other numerical experiments (Schive et al. 2014a,b; Veltmaat & Niemeyer 2016a; Schwabe et al. 2016) reveal just this: ULA/scalar field DM halos comprise a central soliton core transitioning to an NFW-like profile at large radii. The size of the core depends on the axion mass and local density, with larger cores occurring for smaller particle masses and lower densities. Standard CDM halos are well described by the NFW profile at all radii and display a central cusp. For almost a decade now, it has been suggested in that the cusp-core problem in dwarfs, as well as other "small-scale crises" (Weinberg et al. 2015), may be evidence for DM physics beyond CDM(e.g. Bode et al. 2001; Tulin et al. 2013; Marsh & Silk 2014; Vogelsberger et al. 2016; Bull et al. 2016). It is not necessary that a DM model solve all of the apparent small-scale crises at once (a catch-all solution), but proposed solutions to any given problem must, of course, be consistent with cosmology and structure formation.

The stellar dynamics of dwarf spheroidal (dSph) galaxies in the Milky Way (MW) can be used to study the distribution of DM in these systems (see e.g. Walker 2013, for a review). dSphs are DM dominated at all radii, and so the stars can be seen as test particles orbiting in the DM halo. In particular, Fornax and Sculptor galaxies have two distinct stellar sub-populations of different metallicty. (Walker & Peñarrubia 2011) (henceforth, WP11) used the virial quantity $\langle \sigma_{\rm los}^2 \rangle$ to measure the DM density profile slope, and showed a preference for cores ($\rho \propto r^0$) over cusps ($\rho \propto r^{-1}$). Different particle physics models for DM predict different halo profiles; therefore the dSph measurements can be used to test the consistency of these models, or even to give evidence for one model over another (e.g. Strigari et al. 2007). First attempts to use Stellar dynamics of dSphs to constrain axion and scalar field DM models are discussed in e.g. (Diez-Tejedor et al. 2014; Marsh & Pop 2015; Chen et al. 2016)

In this work we address how stellar velocity measurements in dSph's can be used to place *unbiased* constraints to the dark matter particle mass for an axion DM halo model. We investigate this using a series of N-body mocks for stars as test particles orbiting in static DM halos. We identify the now-familiar β-degeneracy, which introduces significant bias in the extraction of halo parameters using Jeans analysis when the stellar velocity anisotropy, β, is unknown. We then show how certain parameters can be extracted in an unbiased way using virial (integrated) quantities, where dependence on the anisotropy is reduced.

Fig. 1 represents our main findings concerning the axion mass and the MW dSphs. A joint Jeans analysis of the velocity dispersion profile of the eight classical MW dSphs (Walker et al. 2010, using the data from) selects a particular axion mass, $m_a = 2.44^{+1.3}_{-0.6} \times 10^{-22}$ eV.[2] However, our analysis of mocks leads us to conclude that the Jeans analysis has an unknown bias in the recovered axion mass, caused

by the β-degeneracy. Notice that the Jeans analysis is also in some tension with the constraints of (Marsh & Pop 2015) (hereafter MP15) based on the mass profile slope and virial mass estimator of WP11, which limits $m_a < 1.1 \times 10^{-22}$ eV at a 95% confidence level (C.L.). We revise this upper limit in a new analysis, proved to work extremely well in mock data, finding $m_a < 0.4 \times 10^{-22}$ eV at 97.5% C.L., using $\langle \sigma_{\rm los}^2 \rangle$ from direct integration of Jeans equation, which we dub the $\langle \sigma_{\rm los}^2 \rangle$-fit.

In the rest of this paper we carefully examine the source of the discrepancy in these bounds on the ULA mass from dSphs, and argue that our revised bound is unbiased. We then discuss possible implications from a cosmological perspective. This paper is organized as follows. We begin in Section 2 by reviewing the status of the cusp-core problem in dSphs. In Section 3 we describe the ULA halo density profile, the model for stellar kinematics, and the set of synthetic observations we use to test our methodology. We perform N-body simulations of stars in the DM potential to generate mock data. In Section 4 we present the results of a Markov Chain Monte Carlo (MCMC) analysis over synthetic observations where we fit the parameters of our model using: (i) the full velocity dispersion profile i.e. Jeans analysis; (ii) the averaged velocity dispersion of two stellar populations using a mass-velocity dispersion estimator, as it was first proposed in (Walker & Peñarrubia 2011) and referred here as the slopes method; and (iii) a variation of the slopes method, the aforementioned $\langle \sigma_{\rm los}^2 \rangle$-fit, where we propose to use an unbiased estimator based on a further integration of the Jeans equation. Then the same three analyses are performed on the real data. We shall see that $\langle \sigma_{\rm los}^2 \rangle$-fit is the only one providing unbiased estimates on the axion mass from the kinematics of dSph's. Section 5 discusses the cosmological (in)consistency of the axion cores, and compares our constraints to other studies. We conclude in Section 6. The Appendix presents some additional details on Jeans analysis, and some discussion of constraints from cosmological reionization.

2 STATUS OF THE DSPHS DATA, THE CUSP-CORE PROBLEM, AND SOLUTIONS

The dSph satellites of the MW are promising objects to test DM models that differ from CDM on small scales. These old, pressure-supported systems are the smallest and least luminous known galaxies, and there is strong evidence that they are DM-dominated at all radii, with mass-to-light ratios as large as (Mateo 1998)

$$M/L_V \sim 10^{1-2} [M/L_V]_\odot . \tag{1}$$

Being the most DM-dominated and metal-poor galaxies in the known Universe (Mateo 1998; McConnachie 2012), dSph galaxies play a fundamental role in galaxy formation models as well as in investigations of the particle nature of DM. Currently, we lack a clear theoretical understanding of the distribution of DM in these objects. While the density profiles of CDM halos found in collision-less N-body simulations are well described by a close-to-universal, centrally-divergent ('cuspy') profile (e.g. Navarro et al. 1997), alternative DM particle models that allow for long-range self-interacting forces (e.g Spergel & Steinhardt 2000; Vogels-

---

[2] While the present work was in preparation, a similar Jeans analysis was performed by (Chen et al. 2016), whose results are broadly consistent with ours. We comment on their analysis later.
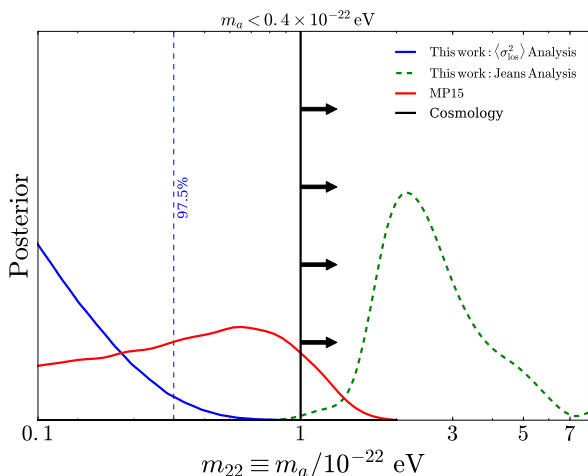
Figure 1. Marginalized constraint on axion mass from dSph stellar dynamics using three methodologies. Using mock data, we demonstrate that only the $\langle\sigma_{\rm los}^2\rangle$-fit returns unbiased results. The constraint from this method, $m_a < 0.4 \times 10^{-22}$ eV, produces too few subhalos and is inconsistent with a conservative bound of $m_a > 1 \times 10^{-22}$ eV from cosmology. Jeans analysis returns the most biased results, due to the anisotropy degeneracy, while the "virial estimator" of WP11 used by MP15 (see text) has a slight bias to larger axion masses.

berger et al. 2012; Kaplinghat et al. 2016) or a small enough DM particle mass (e.g. Tremaine & Gunn 1979; Bode et al. 2001) naturally lead to halo profiles with homogeneous-density 'cores'.

Besides the exotic microscopic properties of DM, a large body of hydro-dynamical simulations suggests that baryons can also reshape the primordial density profiles of dSphs. For example, dense baryonic clumps transfer angular momentum to the DM halo as they decay to the inner-most regions of the galaxy through dynamical friction, erasing the central cusp in the process (El-Zant et al. 2001; Nipoti & Binney 2015). Also, violent periodic fluctuations in the baryonic potential driven by supernova explosions can remove primordial DM cusps (Navarro et al. 1996; Read & Gilmore 2005; Governato et al. 2012; Di Cintio et al. 2014). Although the amount of supernova energy required to transform the halo profile may become prohibitively large in the faintest MW dSphs (Peñarrubia et al. 2012), recently some authors have argued that stochastic star formation in low-mass halos may overcome the energetic limitations, leading to the formation of DM cores of size comparable to the stellar half-mass radii of dSphs if star formation proceeds for long enough (Read et al. 2016). However, other groups using different hydrodynamical codes and feedback recipes do not find DM cores on the mass scale of dSphs at all (Sawala et al. 2016; Zhu et al. 2016); the differences seems to be due to a poorer resolution and modelling of the interstellar medium as compared with e.g. (Read et al. 2016).

The dynamical modelling of dSph galaxies is complicated by the strong degeneracy between the orbital anisotropy of the stellar tracers and the unknown DM distribution in these objects (see Walker 2013, for a review). These degeneracies arise in the modelling of line-of-sight velocities using the spherical Jeans equations (e.g Kleyna et al. 2001; Gilmore et al. 2007; Battaglia et al. 2008; Lokas 2009;

Walker et al. 2009b, 2010; Richardson & Fairbairn 2014), parameterized phase-space distribution functions (Kleyna et al. 2002; Wilkinson et al. 2002; Strigari et al. 2010; Amorisco & Evans 2012; Amorisco et al. 2013), made-to-measure techniques (Long & Mao 2010), as well as orbit-based dynamical models (Jardel & Gebhardt 2013; Jardel et al. 2012; Breddels et al. 2013; Breddels & Helmi 2013).

WP11 devised a simple method for breaking the mass-anisotropy degeneracy in dSphs with multiple chemo-dynamical populations. For a given dSph, WP11 (see also Amorisco & Evans 2012) use measurements of stellar positions, velocities, and spectral indices to estimate half-light radii and velocity dispersions for as many as two chemo-dynamically independent stellar sub-populations. Several works have shown that the mass estimator (Walker et al. 2009b; Wolf et al. 2010)

$$G\,M(< R_{\rm half}) = \mu\,R_{\rm half}\,\langle\sigma_{\rm los}^2\rangle\,, \qquad (2)$$

has a value μ independent of the (unknown) orbital anisotropy of the stellar population. $R_{\rm half}$ is the projected half mass radius, which for a Plummer stellar density profile is related to the three dimensional one by: $r_{\rm half} = 1.305\,R_{\rm half}$, and the luminosity averaged velocity dispersion is defined as

$$\langle\sigma_{\rm los}^2\rangle = \frac{\int_0^\infty \sigma_{\rm los}^2(R')I(R')R'dR'}{\int_0^\infty I(R')R'dR'}\,. \qquad (3)$$

Hence, detection of two distinct sub-populations with different sizes provide mass estimates $M(< R_{\rm half})$ at two different radii in the same mass profile, immediately specifying a slope

$$\Gamma \equiv \frac{\Delta\log M}{\Delta\log R_{\rm half}} = 1 + \frac{\Delta\log\langle\sigma_{\rm los}^2\rangle}{\Delta\log R_{\rm half}}. \qquad (4)$$

For Fornax and Sculptor, WP11 find slopes of $\Gamma = 2.61^{+0.43}_{-0.37}$ and $\Gamma = 2.95^{+0.51}_{-0.39}$, respectively, which are consistent with cored DM potentials, for which $\Gamma \leqslant 3$ at all radii, but incompatible with cusped potentials, for which $\Gamma \leqslant 2$.

However, WP11 also showed that the coefficient μ in Equation (2) is not generally a constant. Tests with mock data reveal that the value of μ varies depending on (i) the spatial segregation of the stellar tracers within the DM halo, and (ii) the DM halo profile itself. In particular, μ increases as the stellar population is more deeply embedded within the dark matter halo, i.e. in the limit $r_{\rm half}/r_{\rm s} \to 0$, and increases more strongly in halos with a shallow density profile. As a result, the values of Γ measured by WP11 must be taken as strict lower limits, which implies that the exclusion levels of cuspy halo profiles in Fornax and Sculptor are conservative. Moreover, because of the non-constancy of μ, using Eq. (2) to fit halo parameters such as the DM particle mass can lead to biased constraints.

3 MODEL AND SYNTHETIC DATA

3.1 The axion halo density profile

In this work we use the density profile found by (Schive et al. 2014a,b; Schwabe et al. 2016; Veltmaat & Niemeyer 2016a; Mocz et al. 2017) from numerical simulations of structure

formation with ULAs (as parameterized in MP15):

$$\rho(r) = \begin{cases} \dfrac{\rho_{\mathrm{sol}}}{\left[1 + (r/r_{\mathrm{sol}})^2\right]^8} & \text{for} \quad r < r_\epsilon \\[3ex] \dfrac{\rho_{\mathrm{NFW}}}{(1 + r/r_{\mathrm{s}})^2 (r/r_{\mathrm{s}})} & \text{for} \quad r \geqslant r_\epsilon \end{cases} . \quad (5)$$

where r_{sol} is the characteristic radius of the soliton core, and ρ_{sol} the central density. The soliton density and radius are related by the axion mass, m_a (Ruffini & Bonazzola 1969; Schive et al. 2014a,b, MP15)[3]

$$r_{\mathrm{sol}} = \left[\frac{\rho_{\mathrm{sol}}}{2.42 \times 10^9 \ \mathrm{M_\odot kpc^{-3}}} \left(\frac{m_a}{10^{-22}\mathrm{eV}} \right)^2 \right]^{-0.25} \mathrm{kpc} \,. \quad (6)$$

The parameters corresponding to the external profile (NFW) are ρ_{nfw} and the scale radius r_{s}. The radius r_ϵ is the transition radius from the soliton (inner) to the NFW profile (external).

We fix the matching radius between the profiles by the density ratio, ϵ, and in turn use this to fix the NFW characteristic density by continuity:

$$\frac{\rho_{\mathrm{sol}}}{\left[1 + (r_\epsilon/r_{\mathrm{sol}})^2\right]^8} = \epsilon\rho_{\mathrm{sol}} = \frac{\rho_{\mathrm{nfw}}}{(1 + r_\epsilon/r_{\mathrm{s}})^2 (r_\epsilon/r_{\mathrm{s}})} \,, \quad (7)$$

We can now rewrite the density profile in the form

$$\rho(r) = \rho_{\mathrm{sol}} \begin{cases} \dfrac{1}{\left[1 + (r/r_{\mathrm{sol}})^2\right]^8} & \text{for} \quad r < r_\epsilon \\[3ex] \dfrac{\delta_{\mathrm{NFW}}}{(1 + r/r_{\mathrm{s}})^2 (r/r_{\mathrm{s}})} & \text{for} \quad r \geqslant r_\epsilon \end{cases} . \quad (8)$$

where

$$r_\epsilon = r_{\mathrm{sol}}(\epsilon^{-1/8} - 1)^{1/2} \,, \quad (9)$$

and

$$\delta_{\mathrm{NFW}} = \epsilon \left[\frac{r_\epsilon}{r_{\mathrm{s}}} \left(1 + \frac{r_\epsilon}{r_{\mathrm{s}}} \right)^2 \right] \,. \quad (10)$$

With this form we can see that the density profile is fully determined once we fix the set of physical parameters: $m_a[\mathrm{eV}]$, $\rho_{\mathrm{sol}}[\mathrm{M_\odot kpc^{-3}}]$, ϵ and $r_{\mathrm{s}}[\mathrm{kpc}]$. Notice that relation (6) implies that only two of the three parameters that defines de soliton, m_a, ρ_{sol} and r_{sol}, are actually independent. In this work we are assuming that there is a universal DM density profile and dSph's galaxies have not been affected on by barionic feedback. Under such assumptions we can set m_a to be a universal free parameter in our analysis. We now have some freedom to choose between ρ_{sol} and r_{sol} to be the

other free parameter. We decided to use ρ_{sol} only because the prior range can be set more intuitively, but as we will show in section 4.2.1 this choice do not affect the results. As we defined the axion mass as a universal parameter, common to all halos, this is essentially a three parameter halo model, with ϵ the additional parameter over a canonical NFW profile. There is no definite theoretical prediction on how to set the matching radius r_ϵ, though it is expected to be of order the de Broglie wavelength of the ULA. In the simulations of (Schive et al. 2014a) the transition typically occurs for $\epsilon \sim 10^{-2}$, with a small redshift dependence. In (Schive et al. 2014b; Schwabe et al. 2016; Veltmaat & Niemeyer 2016a; Mocz et al. 2017), soliton mergers are observed to lead to a core-halo mass relationship that in principle determines ϵ (though details of the results differ somewhat). In practice using a core-halo mass relationship is not efficient for MCMC analysis (as it involves solving an additional integral equation), and so in the present work we take ϵ as a free parameter in each galaxy.[4] In this model the connection between the galactic dynamics and the properties of DM, i.e. the particle mass, is explicit and once we fix the particle mass by any means it must be the same for all the different galaxies in the Universe. On the other hand, the density profile depends on another three parameters that are free to change from galaxy to galaxy. Our expectation is that, observationally at least, ϵ could be correlated with other properties of the cosmological model (e.g. structure formation history), or with the other free parameters of the halo (central density and scale radius). Furthermore, the scaling properties of the soliton suggest ϵ may be independent of the axion mass. In the case that all parameters were constrained by the data, one could then use the inferred posteriors to test consistency with the theoretical core-halo mass relationship and check the consistency of the inferred dSph density profiles with the formation history in simulations. Since this is not the case, we consider it prudent to simply marginalize over the unconstrained degrees of freedom, and focus on constraints to the axion mass.

It is important to state that the purpose of the present work is not to compare the profile in Eq. (8) with other halo models in the literature, but rather to use dSph dynamics to investigate the parameters of the ULA scenario and test its consistency as an explanation for dSph cores.

3.2 Dwarf spheroidal internal dynamics

Walker et al. (2009b); Walker et al. (2007); Mateo et al. (2008); Walker et al. (2009a) reported empirical velocity dispersion profiles for the eight "classical" dSphs of the Milky Way: Carina, Draco, Fornax, Leo I, LeoII, Sculptor, Sextans, and Ursa Minor. Our study extends previous analyses carried out for the generalized Hernquist (Walker et al. 2009b), Burkert (Salucci et al. 2012) and Bose-Einstein condensate (Diez-Tejedor et al. 2014) profiles for the DM halo model in Eq. (8). These studies find that all these types of profile provide good fits to the data. This is due to the strong degeneracy between the mass density profile and the

---

[3] The soliton profile is an equilibrium configuration that is numerically obtained from the so-called Schrodinger-Poisson (SP) system (Ruffini & Bonazzola 1969; Schive et al. 2014a; Guzman & Urena-Lopez 2004), and the expression in Eq. (5) is a quite good fitting formula to the numerical solution. Here we are following the notation in MP15, but also see (Schive et al. 2014b) for an alternative formula. From the original solution of the SP system, the parameters of the soliton profile are explicitly given by: $r_{\mathrm{sol}} = (0.23 m_a \lambda)^{-1}$, and $\rho_{\mathrm{sol}} = m_{\mathrm{Pl}}^2 m_a^2 \lambda^4 / 4\pi$, where m_{Pl} is the Planck mass, and $\lambda < 10^{-3}$ is a scaling parameter (more details can be found in (Ruffini & Bonazzola 1969; Guzman & Urena-Lopez 2004)). Eq. (6) is then obtained from the aforementioned expressions when they are combined to eliminate λ.
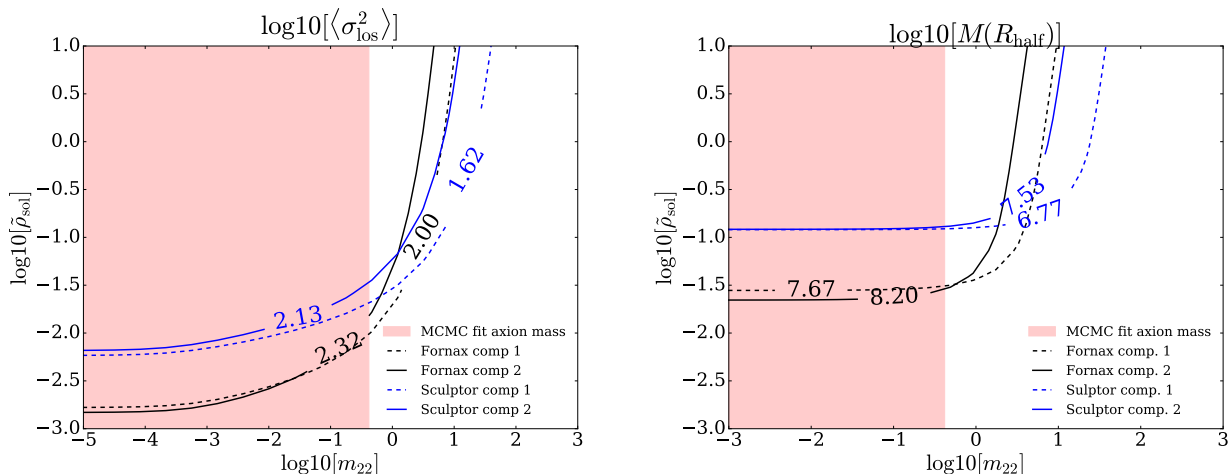
[4] Note that we choose to work with ϵ, instead of r_ϵ, simply because we have a better intuition for the prior: $0 < \epsilon < 1$ in Eq. (9).

Figure 2. (Left) Mean squared velocity dispersion given by Eq. (2),$\langle\sigma^2_{\rm los}\rangle$, for the two observed populations in Fornax and Sculptor galaxies, as a function of the central density and the axion mass. (Right) Enclosed mass within the half mass radius, $M(R_{\rm half})$, as a function of the central density and the axion mass . Contours correspond to the the median values of $\langle\sigma^2_{\rm los}\rangle$ and $M(R_{\rm half})$ reported in (Walker & Peñarrubia 2011). Units: axion mass [10^{-22}eV]; soliton density [$2.42\times 10^9 M_\odot {\rm kpc}^{-3}$]; mass [$M_\odot$] and squared velocity dispersion in [${\rm km^2 s^{-2}}$].

anisotropy of the velocity dispersion. Here we will apply standard methodologies to generate *mock data*, which reveals that without proper knowledge of the true anisotropy, or the true density profile, the use of Jeans analysis leads to biased constraints on the model parameters.

Assuming a constant orbital anisotropy, $\beta(r) = {\rm const}$, the (observed) projection of the velocity dispersion along the line-of-sight, $\sigma^2_{\rm los}(R)$, relates the mass profile, $M(r)$, to the (observed) projected stellar density, $I(R)$ (and the corresponding 3D stellar density $\nu(r)$), through (Binney & Tremaine 2008)

$$\sigma^2_{\rm los}(R) = \frac{2G}{I(R)} \int_R^\infty dr' \nu(r') M(r') (r')^{2\beta-2} F(\beta, R, r'),$$
(11)

See Appendix A for the specific form of the stellar density, I(R), and the function $F(\beta, R, r')$ (only dependent on the anisotropy). In section 4.1.1 we use Eq. (11) to perform a Monte Carlo analysis to infer the parameters from the line-of-sight velocity dispersion profile, i.e. to perform a standard Jeans analysis. This analysis will show the presence of the β-degeneracy, leading to significant bias in Jeans analysis.

A second quantity we will examine, also with the help of the mocks, is the luminosity averaged velocity dispersion, $\langle\sigma^2_{\rm los}\rangle$. Being a virial quantity this has the potential to yield constraints on the DM density profile that are not affected by the β-degeneracy (Walker & Peñarrubia 2011).

The analysis performed in WP11 and MP15 uses the empirical relationship given in Eq. (2), which we call M-estimator, to relate the measured velocity dispersion to the enclosed mass. This relation can be used to set constraints to the model at hand since the density profile, Eq. (5), depends explicitly on the axion mass. However, in WP11 it was also shown that this method tends to systematically overestimate the mass of the inner stellar subcomponent to a greater degree than that of the outer stellar subcomponent, and therefore to underestimate the slope, with the error introduced depending on the particular DM density profile.

Fig. 2 shows that the non-constancy of the virial coefficient μ in Eq. (2) affects the axion mass constraints. We draw contours of constant $\langle\sigma^2_{\rm los}\rangle$ (left) and $M(R_{\rm half})$ (right), fixed to the median values reported in WP11 for each population in Fornax and Sculptor, as a function of the axion mass and the central density. The intersection of the solid and dashed black lines corresponds to the set of parameters that fit the data for Fornax. Since for Sculptor the blue lines do not intersect, it is Fornax that provides the strongest constraint if we attempt to fit both galaxies simultaneously. In this schematic figure we are not considering the confidence interval reported on the WP11 quantities, and so Fig. 2 should not be used to estimate constraints on the halo parameters. The purpose of the figure is to show the difference between fitting the halo parameters using the averaged velocity dispersion or the enclosed mass at half light radius. A comparison of the two panels indicates that a flat prior on the axion mass can lead to different answers depending on what quantity is being used to make the fit. Since in WP11 the observable quantity is $\langle\sigma^2_{\rm los}\rangle$, we shall fit to it directly, rather than use the virial estimator for the enclosed mass. We will show that this choice yields unbiased constraints on the axion mass.

One final remark is that in both panels of Fig. 2 we observe that the axion mass cannot be constrained from below, as the two observables become sensitive to the central density alone as $m_{22} \to 0$. That is, the most we can expect is to find an upper bound on the axion mass and a well constrained central density, which are just consequence of the preference of the WP11 data for large cores.

In section 4.1.2 we test and compare the fits using the M- estimator and the *averaged velocity dispersion*, Eqs. (2) and (3), using mocks of Fornax and Sculptor-like galaxies, each containing two populations of stars with different half-light radii, for different values of the axion mass and central density. The analysis using the M-estimator considers Eq. (2) and the mass obtained from the density profile in Eq. (5) to do Monte Carlo analysis to infer the free pa-

rameters in the axion model. On the other hand, for the Monte Carlo analysis with the averaged velocity dispersion, also to infer free parameters of the axion model, denoted as $\langle\sigma_{\mathrm{los}}^2\rangle$-fit, we use Eq. (11) to compute the squared velocity dispersion profile, σ_{los}^2, and then find the corresponding luminous averaged velocity dispersion as defined in Eq. (3). The integrals in Eqs. (3) and (11) were done using the *quad* routine from the *scipy* library (Jones et al. 01). Since $\langle\sigma_{\mathrm{los}}^2\rangle$ is independent of β we adopt $\beta = 0$ for simplicity, and we have corroborated that this works also well in mocks with non-constant orbital anisotropy (see Fig. 7).

3.3   Generation of mock data

Our model assumes that stars are massless tracers of the DM halo potential, with a spatial distribution chosen so that they describe a Plummer model in equilibrium within the dwarf halo, Eq. A4. For simplicity, we assume that the stellar particles have a phase-space distribution function that is spherically symmetric. Regarding anisotropy we construct two set of mocks, one with $\beta = 0$ (isotropic), and one in which β increases with radius, with as Osipkov-Merrit model. The distribution function is then of the form:

$$f(Q) = \frac{1}{8\pi^2}\left[\int_0^Q \frac{d^2\nu_Q}{d\Psi^2}\frac{d\Psi}{\sqrt{Q-\Psi}} + \frac{1}{\sqrt{Q}}\left(\frac{d\nu_Q}{d\Psi}\right)_{\Psi=0}\right], \quad (12)$$

where $\Psi = -\Phi + \Phi_\infty$, $Q = \varepsilon - L^2/2r_a^2$, and $\varepsilon = -E + \Phi_\infty$. Φ_∞ is an arbitrary constant that guarantees $\varepsilon \geqslant 0$ in the radial range of interest, and Φ is a solution to the Poisson equation $\nabla^2\Phi = 4\pi\rho$, where ρ is given by Eq. (8). Notice that

$$\nu_Q(r) = (1 + \frac{r^2}{r_a^2})\nu(r), \quad (13)$$

and that we recover the isotropic case by having very large values of r_a. An advantage of our density profile model, Eq. (8), is that there exists an analytic solution for the gravitational potential. For a given choice of $\rho(r)$ and $\nu(r)$ we solve Eq. (12) and generate $N_\star = 10^4$ stellar particles with position and velocity vectors $(\mathbf{r}, \mathbf{v})$ in equilibrium within the DM halo potential.

For the axion model we have two sets of mocks, one with isotropic velocity dispersions, $\beta = 0$ and a second one with an Osipkov-Merrit anistropy profile given by:

$$\beta(r) = \frac{r^2}{r_a^2 + r^2}, \quad (14)$$

where r_a is the anisotropy radius, for radius smaller than r_a the velocity dispersion is nearly isotropic, while for larger radius it becomes radially anisotropic. In this second set of mocks we set the anisotropy radius equal to the half mass light radius of the galaxy, i.e $r_a = r_{\mathrm{half}}$. In Tables 1 and 2 we specify the parameters that define the mock data for the axion and NFW models respectively. For the axion model we choose a relatively large mass of $m_a = 2.4 \times 10^{-22}$ eV, consistent with the central value of our joint Jeans analysis performed with the 8 classical dSphs, since we would like to determine under what circumstances this model can be reliably recovered from mocks. We generated mocks for two different half light radii, obtaining the positions and velocities for each population, then this is treated as one single

Name	m_a	ρ_{sol}	r_{sol}	r_s	ϵ	$r_{\mathrm{rhalf}}^{\mathrm{comp.1}}$,$r_{\mathrm{rhalf}}^{\mathrm{comp.2}}$
Mock1						
Fornax	2.44	0.037	1.45	0.39	0.48	0.549,0.891
Sculptor	2.44	0.057	1.3	0.57	0.464	0.167,0.302
Mock2						
Fornax	0.79	0.03	2.66	0.39	0.02	0.549,0.891
Sculptor	0.79	0.1	1.99	0.57	0.06	0.167,0.302
Mock3						
Fornax	0.46	0.017	4.08	2	0.01	0.549,0.891
Sculptor	0.46	0.1	2.62	21	0.01	0.167,0.302

Table 1. Mocks for the axion model. Axion mass and soliton density units are: 10^{-22}eV and $2.42\times10^9 M_\odot\mathrm{kpc}^{-3}$, respectively. Soliton and scale radius,(r_{sol}, r_s), are given in kpc. For these parameters we have two sets of mocks, one with $\beta = 0$, and one with $\beta = r^2/(r_a^2+r^2)$ where $r_a = r_{\mathrm{half}}$. When used as a single population, the half light radius is the mean of the two components.

Name	ρ_{nfw}	r_s	r_{half}
Fornax$_{\mathrm{nfw}}$	0.042	0.49	0.533
Sculptor$_{\mathrm{nfw}}$	0.0182	0.83	0.235

Table 2. Mocks for the NFW profile. Density is give in units of $2.42\times10^9\mathrm{M}_\odot/\mathrm{kpc}^3$ and scale radius in kpc. All mocks uses $\beta = 0$.

data set, for the analysis of method (i), and issused as the two populations for the analysis of methods (ii) and (iii). [5]

4   RESULTS

All our results are obtained using Markov Chain Monte Carlo (MCMC) analysis. We optimize the likelihood function (which we define below) to find the maximum likelihood set of parameters, and use this as the starting point to explore the parameter space and to estimate the confidence intervals for each parameter. For this task we use the publicly available EMCEE code (Foreman-Mackey et al. 2013), an affine invariant ensemble sampler, and allow each chain to run up to convergence as defined by the spectral analysis of (Dunkley et al. 2005).

We first analyze our mocks, and then move on to the real data. In both cases, we fit σ_{los} (Jeans analysis) and $\langle\sigma_{\mathrm{los}}^2\rangle$. Details of the Jeans analysis can be found in Appendix A; while for the $\langle\sigma_{\mathrm{los}}^2\rangle$-fit we use Eq. (3), as well as the M-estimator of Eq. (2).

4.1   Analysis of mock data

4.1.1   Jeans Analysis

In order to fit the mock observations we have four free parameters per galaxy: three associated with the halo model, the central density ρ_{sol}, the density matching ϵ and the scale radius r_s; and one associated with the stellar component, the orbital anisotropy β. In addition, we also have the mass of the axion m_a which in principle should be a global free parameter. However, our first goal is simply to determine how well a Jeans analysis can constrain this parameter in a single

---

[5] Mock data is publicly available to use at the GAIA challenge web page http://astrowiki.ph.surrey.ac.uk/dokuwiki
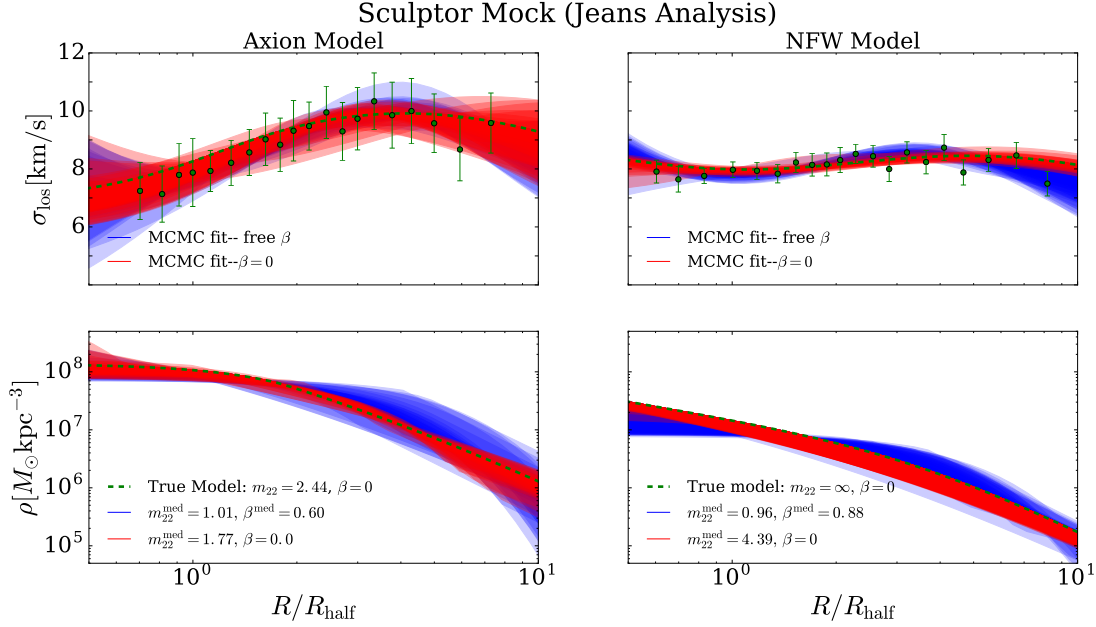
Figure 3. The first row shows the velocity dispersion profile for a Sculptor-like mock with underlying axion (left), and NFW (right) density profiles. For both the axion and NFW mock data we fit the axion profile, Eq. (5), under two separate assumptions: (i) the orbital anisotropy, β, is a free parameter (blue); and (ii) the orbital anisotropy is fixed to its true value, i.e. $\beta = 0$ (red). The second row shows the recovered density profile compared to the true one (green dashed). Note that for the axion density profile a preferred axion mass value is found but it is smaller than the true value, in particular when β is free. For the NFW case with free β we find an axion mass consistent with a large core, i.e. we find a *false core*, demonstrating the β-degeneracy. In both cases, only when we set β to its known value we do recover a density profile close to the true one (green lines). In the NFW mock, the axion model finds the true model as indicated by a power-law density profile $\rho \propto r^{-p}$ with $p > 0$, and a large value of the axion mass. Axion mass is given in units of 10^{-22} eV.
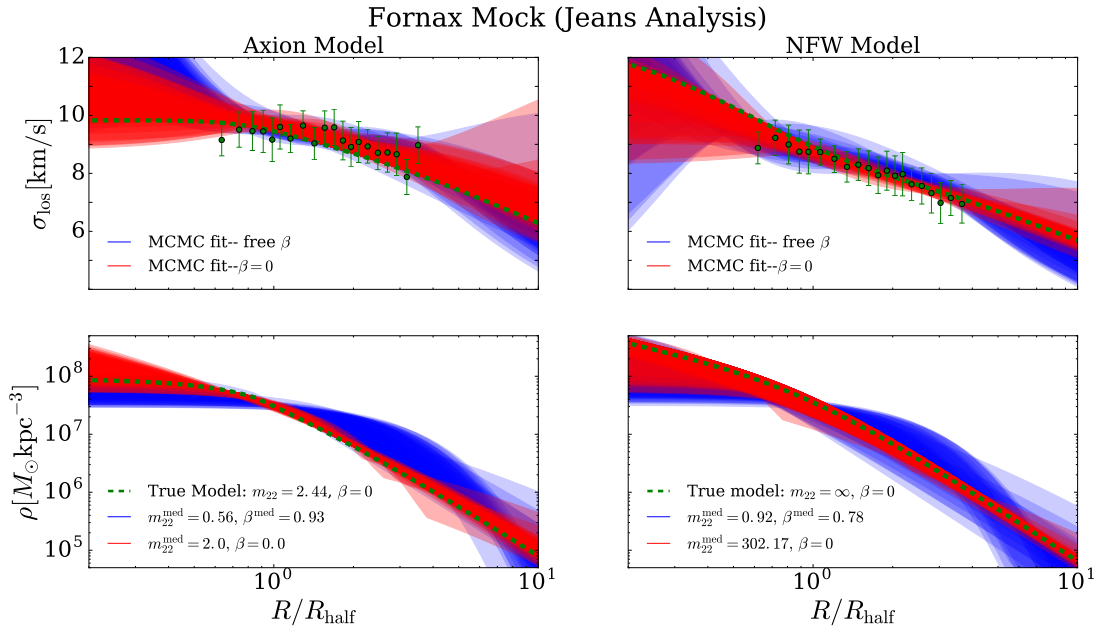

Figure 4. Same as Fig.3 but for a Fornax-like mock. Again a preferred axion mass smaller than the true value is found when β is free (blue). In the case of the NFW mock with free β, we find the presence of a large false core. Only when we set β to its known value (red) do we recover a density profile and parameters close to the true one (green dashed).
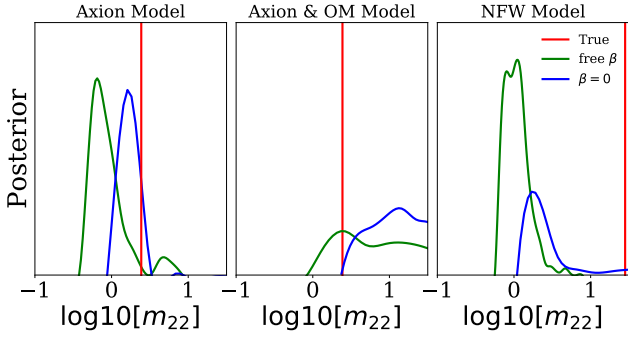
Figure 5. Posterior distribution for the axion mass from the Jeans analysis in the Fornax mocks for the axion with isotropic velocity dispersion(left), the axion with an Osipkov-Merrit anisotropy velocity dispersion profile (middle), and NFW density model with isotropic velocity dispersion (right). For isotropic axion (left) and NFW (right) mocks, the analysis with the anisotropy, β, set as free parameter tends to recover smaller axion mass (note that the NFW profile is similar to an axion one with large axion mass, Eq. (6), so that the core radius goes to zero). For the isotropic axion (left), only when the analysis is done with the true anisotropy, $\beta = 0$, is that we recover an axion mass close to its true value, but still with a significant bias. For the anisotropic axion (middle) we recover a widely spread posterior, even though the maximum of the posterior coincides with the true value. Finally, the NFW isotropic (right) recovers a false core either with the isotropic or the constant anisotropic model.
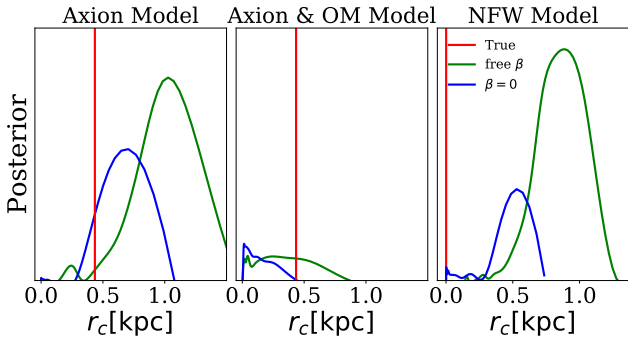
Figure 6. Same as Fig. ?? but the for core radius, $r_c \approx r_{\rm sol}/3$. The analysis with the constant anisotropy, β, set as free parameter tends to recover a larger core for the isotropic mocks (left and right panels). The analysis recover a core radius closer to its true value when the analysis is done with $\beta = 0$, but still with a significant bias. In the case of the axion with an Osipkov-Merrit anisotropy profile (middle panel), the analysis either with $\beta = 0$ or free $\beta = $ const., leads to very spread posterior distributions. In the case of anisotropic Osipkov-Merrit mock it is interesting to notice how the bias is towards smaller core radii, instead to large core radii, as opossed to the bias in the isotropic mocks.

galaxy, and so we treat the axion mass as an additional independent parameter. We define the likelihood function as:

$$\mathcal{L}(m_a, \theta | \sigma) = \prod_{j=1}^{N} \frac{\exp\left[-\frac{1}{2}\frac{\left(\sigma_{\rm obs}(\mathbf{R_j})-\sigma_{\rm los}(\mathbf{R_j},\mathbf{m_a},\theta)\right)^2}{\text{Var}[\sigma_{\rm obs}(\mathbf{R_j})]}\right]}{\sqrt{2\pi\,\text{Var}[\sigma_{\rm obs}(\mathbf{R_j})]}}. \quad (15)$$

where $\theta = (\rho_{\rm sol}, \epsilon, r_{\rm s}, \beta)$ is the vector of parameters describing the halo model. The index j labels the data bins that runs from 1 to the total number of bins N. Here $\sigma_{\rm obs}(R_j)$ is the observed line-of-sight velocity dispersion at projected radius R_j, $\sigma_{\rm los}(R_j, m_a, \theta)$ is given in Eq. (11), $\text{Var}[\sigma_{\rm obs}(R_j)]$ is the square of the error associated with the observed value of the velocity dispersion at R_j. See Appendix A for more details.

Results are shown in Figs. 3 and 4. In summary: Jeans analysis fails to recover the true density profile (dashed green lines) unless the correct value of the anisotropy is adopted (red lines). Using the axion model and allowing the anisotropy to be a free parameter, the Jeans analysis generically infers larger cores than the input ones (blue lines), even recovering a core in the case of an NFW input. This can be seen more clearly in Figure ?? and 6, where we show the posterior distribution for the axion mass and the core radii respectively (right and leftt panels). Even in the case where we use the axion model to fit the axion mock data (left panels in Figs. 3 and 4) and the correct input $\beta = 0$, the Jeans analysis still finds an offsetted posterior on the axion mass, see Fig. 6, although in this case the true value is within 1-sigma level. In addition, in the middle panels of Figures ?? and 6 we show the result for the same analyis but performed over the mock with an Osipkov-Merrit velocity dispersion profile, which is anisotropic. We can see in this case, the analysis with free constant β could recover the truth mass since the maximum of the posterior coincides with it, but this will be only at the expense of using a particular prior. On the other hand, the analysis with $\beta = 0$ tends to recover a rather larger axion mass, and consequently a smaller core radius. In the Osipkov-Merrit mocks the resultant bias is towards larger masses whereas in the isotropic mocks the bias is towards smaller masses. This leave us with the conclusion that in real data a Jeans analysis would lead to biased constraints due to the degeneracy between the mass profile and the anisotropy profile.

4.1.2 Averaged velocity dispersion

Now let us analyze the mocks for the axion model, but using the method outlined in WP11. First we will apply the method as it was originally proposed, using only Eq. (2), which we label as M-estimator. We use the data as reported in WP11 where there is also a variance reported. We the use Eq. (2), together with our model, Eq. (8) to make the comparison with data. Second we will adapt the WP11 method to use Eq. (3) together with Eq. (11), labeled as $\langle\sigma^2_{\rm los}\rangle$-fit. It is important to stress the difference lays in the way we compute the predicted value of $\langle\sigma^2_{\rm los}\rangle$, in the first case we do it through the estimator given in Eq. (2), and in the second one we compute it from a full integration of Jeans equations. In both cases we do a joint analysis of the two populations in each galaxy. We define the likelihood function as:

$$\mathcal{L}(m_a, \theta | \sigma) = \prod_{gal.}\prod_{j=1}^{2} \frac{\exp\left[-\frac{1}{2}\frac{\left(\langle\sigma^2_{\rm obs}\rangle_{\rm pop_j}-\langle\sigma^2_{\rm los}(m_a,\theta_{gal})\rangle_{\rm pop_j}\right)^2}{\text{Var}[\langle\sigma^2_{\rm obs}\rangle_{\rm pop_j}]}\right]}{\sqrt{2\pi\,\text{Var}\langle\sigma^2_{\rm obs}\rangle_{\rm pop_j}}}. \quad (16)$$

where in this case $\theta_{gal} = (\rho_{\rm sol}, \epsilon, r_{\rm s})$ is the vector of parameters describing the halo model of each galaxy. Since we are only using the data from two galaxies, we have 7 free parameters, namely: the axion mass, m_a; the central density of each galaxy, $\rho_{\rm sol}^{\rm For}$, $\rho_{\rm sol}^{\rm Scl}$; and the matching scale and scale radius for each galaxy, $\epsilon^{\rm For}, \epsilon^{\rm Scl}, r_s^{\rm For}, r_s^{\rm Scl}$. The last four parameters tend to be completely unconstrained (consistent with the analysis of MP15), and therefore we will not include them in the triangle plots of posteriors, nor in the discussion.

Results are presented in Fig. 7 where we show the posterior distribution for the axion mass for the three different sets of mocks, in the isotropic (left) and the anisotropic cases (right). From left to right, each mock corresponds to a model with larger axion mass, i.e. a smaller core, see Table 1. First, notice that the M-estimator (green lines) tends to over-estimate the axion mass, although the true value is within the 2-sigma confidence level. We verified that the same conclusion holds when we do not consider the exterior NFW part of the density profile. Second, notice that allowing for broad prior ranges (larger than in MP15) the posterior exhibits a sort of bimodality for the axion mass, which becomes less relevant as the core size (axion mass) increases (decreases). This implies that this method of using two populations will fail to constrain the axion mass if the core size is much smaller than the half-light radius of the dwarf. See Appendix B for more details. Third, we want to stress that our improvement to the method works well independently of the anisotropy of the mocks. These results, together with the information we gather from Fig. 2, demonstrate that for the real data we should fit our model parameters directly to the mean velocity dispersion for the two populations in order to obtain posteriors with the least bias.

4.2 Analysis of Milky Way Dwarf Spheroidals

4.2.1 *Jeans analysis using the eight classical dSph's*

Despite the bias introduced by the β-degeneracy, we present here for completeness the results of Jeans analysis of real stellar dynamical data of the eight classical dSphs. We performed two such analyses: the first treated each dSph individually ("individual analysis"), and the second treated all eight classical dSphs as a single dataset ("joint analysis"). In the joint analysis, each dSph was treated with equal weight in the likelihood function, the axion mass was treated as a universal parameter, and the density profile was taken to have a universal form (effectively assuming that stellar feedback plays no significant role in dSphs of different luminosity). For the individual analysis we used the likelihood from Eq. (15), while for the joint analysis we constructed also a joint likelihood given by the product of the individual likelihoods, one product term for each galaxy.

For brevity we present the results of these analyses for the halo parameters of Fornax alone. The results are shown in Fig. 8. In the individual analysis, the outer (NFW) part of the density profile is unconstrained, and so we show only the parameters constrained by the individual analysis, namely $\{m_a, \rho_{\rm sol}, \beta\}$. In the combined analysis the presence of smaller and larger dSphs that prefer different values of m_a leads to significant broadening of the posterior distributions compared to the individual analysis.

The individual analysis shown in Fig. 8 is consistent with the equivalent analysis (performed while the present work was in preparation) by (Chen et al. 2016), giving the same central values for β and m_a. This shows that the methodological differences between the analyses (parameterization of the halos, stellar density profiles, anisotropy model, and MCMC methodology) do not lead to significant change of the posterior distributions.

As in (Chen et al. 2016), both our individual and combined analyses show well constrained values of β, consistent with $\beta = 0$. However, this *does not mean that the β-degeneracy has been broken.* The limit of the axion density profile to NFW as $m_a \to \infty$ does not allow the Jeans analysis to distinguish cusped from cored profiles, as we demonstrated using mock data in Figs. 3 and 4. Due to the β-degeneracy, Jeans analysis returns small mass values, and large core sizes, even in the case that the NFW profile is the correct one. The results in Fig. 8 should not be read at face value as constraints on the axion mass or core size.

### 4.2.2 *Averaged velocity dispersion of Fornax and Sculptor*

Here we use again the likelihood defined in Eq. (16), with the data obtained from WP11 for Fornax and Sculptor galaxies. Fig. 9 shows the results for our fit using the unbiased $\langle \sigma_{\rm los}^2 \rangle$-fit, in the joint analysis of Fornax and Scultor. We also performed this analysis using the M-estimator (not shown) and found results consistent with those of MP15. The internal kinematics of Fornax and Sculptor only give an upper limit on the axion mass, giving a constraint of $m_a < 0.4 \times 10^{-22}$ eV (97.5% C.L.) using the $\langle \sigma_{\rm los}^2 \rangle$-fit. As expected based on our analysis of the mocks, the new constraint is shifted towards smaller values of the axion mass and central densities compared to the M-estimator used in MP15. The shift in central density is understood as a consequence of the non-constancy of the virial factor with respect to the model parameters, as demonstrated in Fig. 2.

As also anticipated form the mocks, the limits we find are slightly sensitive to the lower bound of the axion mass prior. However, even considering a 3-sigma level for the upper limit, the $\langle \sigma_{\rm los}^2 \rangle$-fit still finds significantly tighter bounds on m_a than MP15. Note also that for this analysis we kept only the soliton part of the model, for which the relevant parameters are m_{22} and $\rho_{\rm sol}$, since the exploration with mocks showed that the rest of the free parameters in Eq. (5) are totally unconstrained.
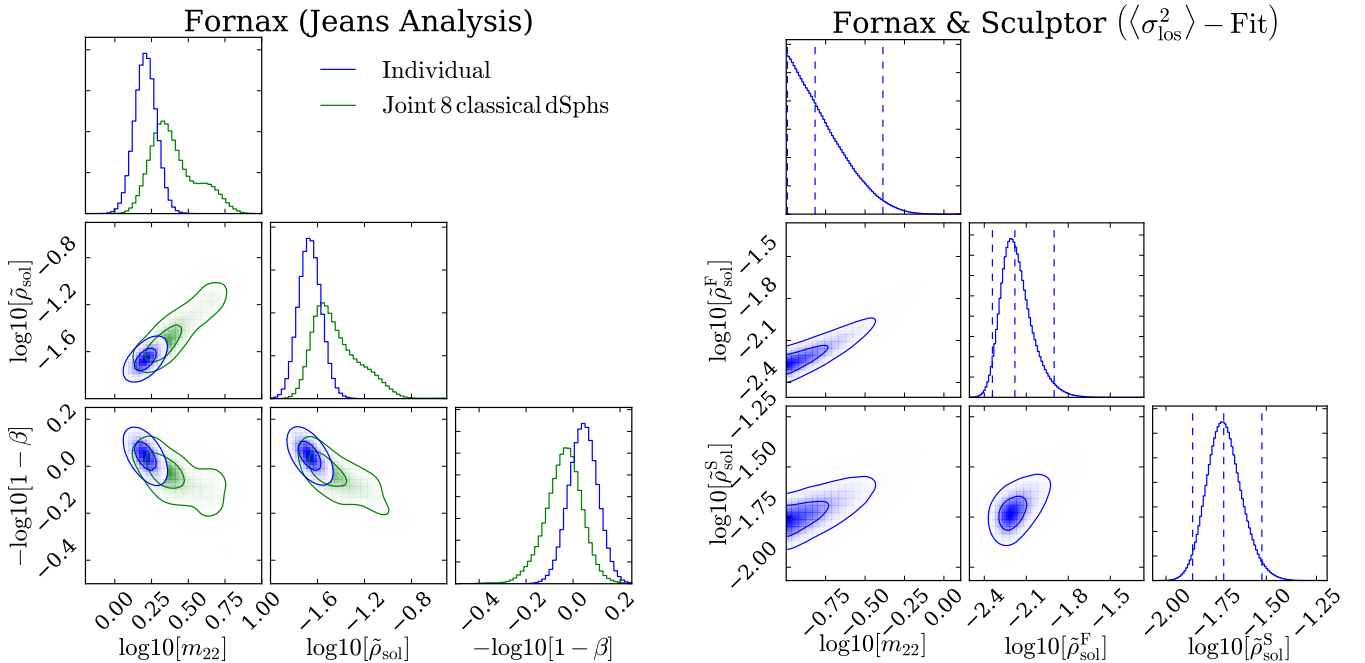
It is important to stress again that our mocks indicated that the $\langle \sigma_{\rm los}^2 \rangle$-fit is unbiased with respect to the axion mass using the method of WP11. The mocks further demonstrate that if the true axion mass were $m_a = 2.4 \times 10^{-22}$ eV, as inferred by the combined Jeans analysis, then the $\langle \sigma_{\rm los}^2 \rangle$-fit should recover this well. Since this was not the case, and we recovered an upper limit inconsistent with the Jeans analysis (see Fig. 1), we must infer that the constraint on the axion mass from Jeans analysis of dSphs is significantly biased to incorrect values due to the β-degeneracy.

5 DISCUSSION

The constraint we find in section 4 requires axion DM to be extremely light, which has very important consequences for

Slope analysis on isotropic mocks

Slope analysis on Osipkov-Merrit mocks
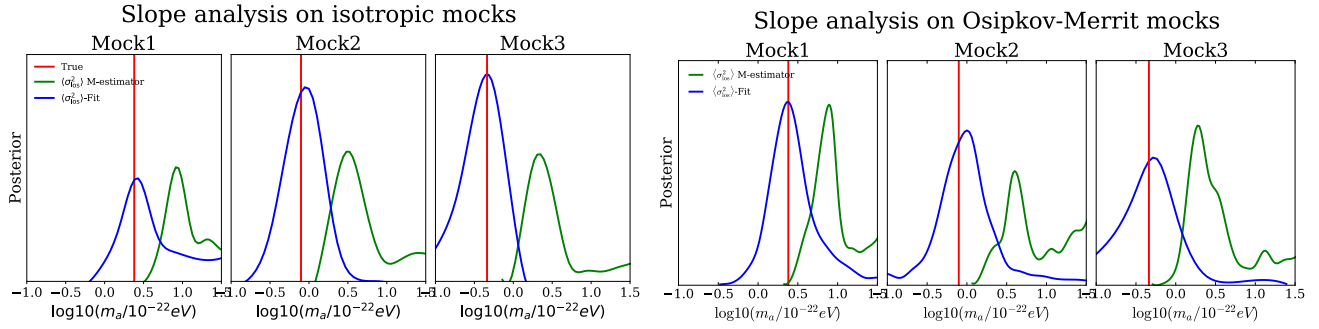
Figure 7. Analysis of three sets of mocks for two stellar populations in Fornax and Sculptor-like galaxies, with two different considerations for the orbital anisotropy: $\beta = 0$ (left) and the Osipkov-Merrit profile (right). Green contours use the constant virial factor M-estimator, Eq. (2) with $\mu = 2/5$, and blue contours use the $\langle\sigma^2_{\rm los}\rangle$-fit, Eq. (3). Both estimators recover central axion mass values close to the input (red line), and demonstrate some bimodality when the prior mass range is large (see Figs. B1 and B2 for the full posterior range). The M-estimator has a noticeable bias to larger axion masses, while the $\langle\sigma^2_{\rm los}\rangle$-fit recovers an unbiased value.

Fornax (Jeans Analysis)

Fornax & Sculptor $\left(\langle\sigma^2_{\rm los}\rangle - {\rm Fit}\right)$

Figure 8. Parameters constrained by the individual Jeans analysis of Fornax, compared to their values in the joint analysis of all eight classical dSphs, where the axion mass is treated as a single universal parameter. Contours show 1 and 2-σ confidence levels. The joint analysis shifts and broadens the axion mass posterior, caused by a "compromise" value between the many galaxies. However, due to the β-degeneracy *the results of this analysis should not be read at face value*. axion mass and soliton density units are 10^{-22}eV and $2.42 \times 10^9 M_\odot {\rm kpc}^{-3}$, respectively

Figure 9. Posterior distribution of the central density and axion mass for the joint analysis of Fornax and Sculptor using the $\langle\sigma^2_{\rm los}\rangle$-fit. Compared to MP15 (which used the M-estimator, see Fig. 1), using the $\langle\sigma^2_{\rm los}\rangle$-fit leads us to find a significant shift in the inferred value of axion mass towards smaller values with a *very tight* bound: $m_a < 0.4 \times 10^{-22}$ eV (97.5% C.L.).The reason for the shift in the inferred axion mass between the two estimators is explained in Fig. 2 by the non-constancy of the virial factor with respect to the model parameters. Contours show 1 and 2-σ confidence levels. axion mass is given in units of 10^{-22}eV and soliton density in units of $2.42 \times 10^9 M_\odot {\rm kpc}^{-3}$.

cosmology. Axion DM suppresses structure formation relative to CDM, and if it is too light it may be in conflict with observations (e.g. Khlopov et al. 1985; Marsh & Ferreira 2010).

5.1 The Number of MW Satellites

In order to assess whether our constraint is consistent with cosmological models, we perform two simple estimates of the

subhalo mass function based on the axion linear mass power spectrum (we use AXIONCAMB Hlozek et al. 2015; Hložek et al. 2016; Lewis et al. 2000);[6] and the halo mass function of

---

[6] AXIONCAMB produces equivalent results to the CLASS (Blas et al. 2011) based code of (Ureña-López & Gonzalez-Morales

(Sheth & Tormen 1999). The first estimate uses the scale-dependent barrier for axions of Marsh & Silk (2014), the approximate progenitor mass function of (Barkana & Loeb 2004), and the subhalo mass function of (Giocoli et al. 2008). The second is based on the method in Schneider (2016); Murgia et al. (2017).[7]

These calculations return an un-normalized mass function for subhalos of mass M in a parent halo of mass M_0, $n_{\rm sub}(> M|M_0)$. For $M_0 = 10^{12} M_\odot \approx M_{\rm MW}$, where $M_{\rm MW}$ is the mass of the Milky Way, the ULA subhalo mass function is equivalent to CDM for large M. Therefore, we normalize our mass function by applying a constant multiplicative factor such that the CDM mass function computed in this manner matches N-body simulation results. We normalize to Lovell et al. (2014), who found $n_{\rm sub}(> 10^{10} M_\odot | M_{\rm MW}) \approx 10$ for CDM, and apply the same normalization factor to the ULA models.

In both calculations we find that ULAs consistent with corrected slopes analysis produce far too little substructure to be consistent with the observations: $m_{22} < 0.4$ cannot even give the eight classical dSphs, never mind passing a more realistic bound such as $n_{\rm sub.} \gtrsim 66$ (Lovell et al. 2014). The subhalo mass function for $m_{22} < 0.4$ turns over and produces no subhalos with $M \gtrsim 10^{9-10}$, which is in conflict with substructure bounds from tidal streams (Bovy et al. 2017). These observations indicate that ULAs may suffer from a similar *Catch 22* to Warm Dark Matter (WDM): if you want cores, you don't get enough satellites; if you want enough satellites, you don't get big enough cores. The two calculations of the subhalo mass function we have considered differ by a factor of a few for larger ULA masses, pointing to the need for improved calculations and simulations to derive accurate conclusions.

The full excursion set calculation for the subhalo mass function with axion DM was recently performed by Du et al. (2017). The excursion set calculation of Du et al. (2017) leads to a *larger* cut-off scale on the halo mass function for fixed axion mass, with the qualitative effects being consistent with our approximate treatments. Thus in the full calculation there will be even less substructure than we have estimated, strengthening our conclusion that ULAs able to provide large cores to Fornax and Sculptor will struggle to produce the observed number of MW satellites (they "over-solve" the "missing satellites" problem). The inability of the subhalo mass function to produce enough satellites does not necessarily exclude the ULA model, however: the mass function gives the expected number, and it could be that the MW is an outlier. There are analytic tools available that use extreme value statistics to compute exclusions based on the most massive objects (e.g. Davis et al. 2011, and references therein), and these could be extended to the lower end of the mass function.

Ultimately, the ULA subhalo mass function should be obtained in MW zoom-in simulations, as was done for WDM by e.g. (Lovell et al. 2014; Bozek et al. 2016). Codes capable of such simulations of ULAs have now been developed by

---

2016), and at low redshifts also matches the analytic transfer function of (Hu et al. 2000).

[7] We thank Riccardo Murgia for providing the code for the second calculation.

Schwabe et al. (2016) and Veltmaat & Niemeyer (2016b). Simulations will quantify the scatter around (semi-) analytic results for the mass function, such as Press-Schechter. Zoom-in simulations will also allow us to study the effect of tidal disruption, which for cored density profiles might be as important as an initial cut-off on the mass power spectrum. This has been recently investigated in (Errani et al. 2017), where they analyze how the number of substructures, in a Milky Way like galaxy, is affected when falling into the disc potential, depending on their initial density profile. They find that the survival of cuspy satellites is almost twice larger than the cored ones. For the axion model, the inverse relation between the central density and the core radius, could lead to a different conclusion, but, once again, simulations are required to say how axion DM halos will respond to the dynamical interaction with baryons. The "quantum" stripping discussed in Hui et al. (2017) will also play an important role.

5.2 Other Constraints

Here we discuss wider implications of our finding, $m_{22} < 0.4$, showing how the dSph stellar kinematics are complementary to other probes of DM. The first observable we want to discuss is CMB, which has been thoroughly studied in ULAs models. Taken at face value, however see section 5.3, our bound is consistent with the current constraints from precision cosmology, in the form of the *Planck* temperature power spectrum, which requires $m_a \gtrsim 10^{-24}$ eV (Hlozek et al. 2015), and it may well be tested to a higher precision in the near future by the lensing power spectrum measured by CMB polarisation Stage-IV ground based telescopes (Hložek et al. 2016).

Interestingly, our inferred mass limit is consistent with the interpretation of ULA quantum pressure as the origin of the offset between dark and ordinary matter in Abell 3827, which requires $m_a \approx 2 \times 10^{-24}$eV (Paredes & Michinel 2016). Our bound is also consistent with constraints based on the survival of the cold clump in Ursa Minor and distribution of globular clusters in Fornax, which require $m_a \sim 0.3 - 1 \times 10^{-22}$ eV (Lora et al. 2012). On the other hand, our bound is in $\gtrsim 2\sigma$ tension with the earlier Jeans analysis of Fornax by (Schive et al. 2014a), $m_a = 8.1^{+1.6}_{-1.7} \times 10^{-23}$ eV (though for the reasons explained, Jeans analysis in this case leads to biased results). Explaining the half-light mass in the ultra-faint dwarfs requires a somewhat larger ULA mass of $m_a \sim 3.7 - 5.6 \times 10^{-22}$ eV (Calabrese & Spergel 2016), which is also in tension with our bound, as is the estimation $m_a \sim 10^{-21}$ eV in (Urena-Lopez et al. 2017), though the errors are large and hard to fully quantify.

Next, we want to compare with constraints from reionization. In this case the comparison is more complicated because the physics of the baryons plays a very important role. Establishing such bounds rigorously, in any given model of DM, requires dedicated studies of the evolution of the mass power spectrum in the quasi-linear regime and modeling of the intergalactic medium (IGM). Some work along these lines has been done by (Bozek et al. 2015) and (Sarkar et al. 2016). The limit on ULA mass from our analysis of the dSph data, $m_{22} < 0.4$, gives a considerable small value for the CMB optical depth, τ, which is in tension with the Planck+ Low-l WMAP 9 (Planck + WP) constraints on τ,

yet this is consistent with the Planck High Frequency Instrument (Planck+HFI) constraint. This demonstrates the power that future constraints on the epoch of reionization from CMB polarization will have to probe the nature of DM (e.g. Calabrese et al. 2014), and the importance of understanding possible low-ℓ polarization systematic errors that could be causing a tension between *Planck* and WMAP τ measurements. See appendix C for wider explanation on how we derived these constraints based on Bozek et al. (2015).

(Sarkar et al. 2016) finds that $m_a > 2.6 \times 10^{-23}$ eV is consistent with their reionization model based on N-body simulations demanding an ionized fraction of HI of 50% by $z = 8$ ($m_a > 10^{-23}$ eV from collapsed mass fraction inferred from Lyman-α absorbers). Our bound is also inconsistent with the Hubble Ultra Deep Field UV-Luminosity function (Bouwens et al. 2015), and a compilation of UV-luminosiy function data (Corasaniti et al. 2017), which both require $m_a \gtrsim 10^{-22}$ eV.

The strongest constraints on any possible suppression of clustering power relative to CDM are found from the Lyman-α forest flux power spectrum. Recently, two groups have performed Lyman-α simulations with ULAs, finding the constraints $m_{22} \gtrsim 20-30$, depending on the exact combination of data used (Armengaud et al. 2017; Iršič et al. 2017). It is important to note, however, that Lyman-α constraints depend strongly on the modelling of the temperature of the intergalactic medium, and in particular can be loosened if the evolution is non-monotonic (Garzilli et al. 2015; Hui et al. 2017).

5.3 The role of feedback and measurements on other dSphs

The main assumptions in this paper is that there is a universal density profile, and that the axion mass can be treated as universal parameter. Such conditions are only consistent if processes associated to the presence of a barionic component, stellar feedback particularly, affects dSph density profiles minimally. Unfortunately, as far as we know, there do not exist simulations of the axion model studying how feedback acts on scalar field halos like those we study.

For the sake of discussion, imagine separating the axion halo into the soliton, which responds as a coherent field, and the NFW piece, which is incoherent and responds as CDM. What we can guess about the effects of feedback based on existing work depends on how big the core of the galaxy is. If the actual axion mass is large, the "true core is small, and feedback will act on the outer part of the halo, creating a "false core out of this initially NFW-like piece, if this external part actually behaves as CDM. In this case, just as for CDM, dSph density profiles will not be universal, and the (luminosity-dependent) effects of feedback will be seen(Read et al. 2016; Sawala et al. 2016; Pontzen & Governato 2014; Governato et al. 2012; Sawala et al. 2010). However, if the axion mass is small, and is itself responsible for the large cores in dSphs, then feedback will act mostly on the soliton piece. In this case, because the soliton is the ground-state of axion DM, the halo relaxes back to the universal profile under perturbations. Numerical simulations indicate that the relaxation time, even for strong perturbations, is of order $t_{\mathrm{rel.}} \sim 10^3/m_a \sim 10^3 m_{22}^{-1}$ years (Guzmán & Ureña-López

2006).[8] According to these studies, the relaxation time for our benchmark axion mass is vanishingly small in astrophysical terms. As long as the last feedback event (e.g. supernova explosion) of relevance occurred some time $t_{\mathrm{feed.}} > t_{\mathrm{rel.}}$ ago, then the soliton will have relaxed back to the groundstate, and the measured $(\rho_{\mathrm{sol.}}, r_{\mathrm{sol.}})$ can be used to reliably infer the axion mass.

The above argument suggests a powerful probe to test the axion model as an explanation of dSph cores versus the need for feedback. If the axion explanation for cores is correct, then our discussion of relaxation times suggests that feedback cannot affect the universal nature of the density profile. Using multiple dSphs, each with multiple stellar populations, this universal nature can be tested. The current constraints from Fornax and Sculptor cannot be used to infer whether the density profile is universal: both galaxies are cored and the size of the core is not bounded from above, and we thus only obtain an upper limit on the axion mass. However, by measuring multiple populations in more dSphs, it may be possible in future to test the universal profile. If future measurements do not find a universal profile, or find inconsistent limits on the axion mass (for example, a large lower limit from a faint, cuspy, dSph), then axions cannot be the sole explanation for dSph cores, and feedback (or some other new DM physics) must be operative. From our tests with mocks (not shown here) we think that the ideal scenario would be a galaxy where two populations are identified and they have such half mass radius that one is very well embedded in the soliton (core), and the other probes the outer part of the DM halo. In this way we would be able to find an axion mass bounded from above and below.

6 CONCLUSIONS

We used mocks of dSphs embedded in an axion DM halo to test for the presence of bias in constraints to the particle mass in axion DM models. The main points to conclude are:

• Using Jeans analysis with constant unknown anisotropy to fit the line of sight velocity dispersion leads to biased constraints on the axion mass, to the point where one can conclude that galaxies are well fitted by the axion halo model (cored) when in reality the underlying model is a "cuspy" one.

• We also found that using the M-estimator to fit the slope defined by the mean velocity dispersion from two different stellar populations in the same galaxy also leads to biased constraints, though to a lesser extent. As expected, the bias is worse when the axion mass is smaller since this case corresponds to very large cores.

• An intermediate approach where we compute the mean velocity dispersion from direct integration of the Jeans equation, Eq. (3), and fit the luminosity averaged velocity dispersion of two stellar subpopulations seems to provide unbiased constraints on the halo parameters.

Fitting $\langle \sigma_{\mathrm{los}}^2 \rangle$ rather than using the M-estimator (used by MP15) in the joint analysis for data from Fornax and

---

[8] Rapid relaxation is also observed in violent events, such as multi-soliton mergers (Schwabe et al. 2016).

Sculptor galaxies taken from WP11 leads to a tighter limit to the axion mass, $m_a < 0.4 \times 10^{-22}$ eV. We have corroborated that our new approach works very well independently of the true anisotropy profile, by applying it to isotropic and anisotropic mock data. This is clearly in tension with a "blind" Jeans analysis, performed using a joint likelihood of the eight classical dSph's, with free constant anisotropy parameter β, which gives $m_a = 2.4^{+1.3}_{-0.6} \times 10^{-22}$ eV. However, our analysis of mocks leads us to believe that the estimate of m_a from Jeans analysis suffers from significant bias, see Fig. 1 for a comparison. Without proper knowledge of the dSph velocity anisotropy it is not possible to extract unbiased constraints on DM models. Here are two important points to remark. First, we are not attempting to extract more information from the other dSphs because we cannot be certain that those galaxies actually have a cored density profile. Second, we have verified that constraints set individually from Fornax and Sculptor are compatible, otherwise stating a joint likelihood would not be correct. From the $\langle \sigma^2_{\rm los} \rangle$ individual fit we obtained $m_{22} < 0.48$ and $m_{22} < 0.79$ for Fornax and Sculptor respectively.

The tight bound on $m_a < 0.4 \times 10^{-22}$ eV required if ULAs are to provide kpc-scale cores to Fornax and Sculptor (WP11 cores) runs into several problems when faced with cosmology. Firstly, we performed a simple estimate of the subhalo mass function, and demonstrated that such a ULA cannot provide enough dwarf satellites of the MW to be consistent with observations. This suggest that ULAs, like WDM, may suffer from a *Catch 22* in that "if you want large cores, you don't get enough dwarfs; if you want enough dwarfs, you don't get big enough cores". Existing cosmological bounds also appear to rule out a ULA origin for the WP11 cores: high-z galaxies rule out $m_a \lesssim 1 \times 10^{-22}$ eV (Bozek et al. 2015; Schive et al. 2016). Constraints from reionization, such as the CMB optical depth τ, are less conclusive, and may even favour low axion mass. If ULAs satisfying our bound are indeed the DM, they can be definitively ruled out either by proper analysis of existing Lyman-α forest power spectrum data (Armengaud et al. 2017), or by upcoming CMB Stage-IV lensing power spectrum measurements (Hložek et al. 2016). However, we would like to emphasis the need of detailed studies of the interplay between the physics of the axion DM and the physics of baryons, in order to make more consistent comparisons.

Improvements on DM constraints from stellar kinematics may be obtained from future measurements of proper motions (e.g. Strigari et al. 2007). Extending our present analysis (chemodynamical modelling of multiple stellar populations combined with the $\langle \sigma^2_{\rm los} \rangle$-fit) to other dwarfs beyond Fornax and Sculptor can be achieved by multi-object spectrographs attached to several-metre telescopes. On a short time scale we have WEAVE(Dalton et al. 2014), MOONS (Cirasuolo et al. 2012) and 4MOST (de Jong et al. 2012). Using these data and our methodology could significantly improve our ability to test models of DM using stellar dynamics.

REFERENCES

Amorisco N. C., Evans N. W., 2012, MNRAS, 419, 184
Amorisco N. C., Agnello A., Evans N. W., 2013, MNRAS, 429, L89
Arbey A., Lesgourgues J., Salati P., 2001, Phys. Rev., D64, 123528
Armengaud E., Palanque-Delabrouille N., Yèche C., Marsh D. J. E., Baur J., 2017, preprint, (arXiv:1703.09126)
Barkana R., Loeb A., 2004, ApJ, 609, 474
Battaglia G., Helmi A., Tolstoy E., Irwin M., Hill V., Jablonka P., 2008, ApJ, 681, L13
Bennett C. L., et al., 2013, ApJS, 208, 20
Binney J., Tremaine S., 2008, Galactic Dynamics: Second Edition. Princeton University Press
Blas D., Lesgourgues J., Tram T., 2011, J. Cosmology Astropart. Phys., 7, 34
Bode P., Ostriker J. P., Turok N., 2001, ApJ, 556, 93
Bouwens R. J., et al., 2015, ApJ, 803, 34
Bovy J., Erkal D., Sanders J. L., 2017, MNRAS, 466, 628
Bozek B., Marsh D. J. E., Silk J., Wyse R. F. G., 2015, MNRAS, 450, 209
Bozek B., Boylan-Kolchin M., Horiuchi S., Garrison-Kimmel S., Abazajian K., Bullock J. S., 2016, MNRAS, 459, 1489
Breddels M. A., Helmi A., 2013, A&A, 558, A35
Breddels M. A., Helmi A., van den Bosch R. C. E., van de Ven G., Battaglia G., 2013, MNRAS, 433, 3173
Bull P., et al., 2016, Physics of the Dark Universe, 12, 56
Calabrese E., Spergel D. N., 2016, MNRAS, 460, 4397
Calabrese E., et al., 2014, J. Cosmology Astropart. Phys., 1408, 010
Chen S.-R., Schive H.-Y., Chiueh T., 2016, preprint, (arXiv:1606.09030)
Cirasuolo M., et al., 2012, in Ground-based and Airborne Instrumentation for Astronomy IV. p. 84460S (arXiv:1208.5780), doi:10.1117/12.925871
Corasaniti P. S., Agarwal S., Marsh D. J. E., Das S., 2017, Phys. Rev. D, 95, 083512
Dalton G., et al., 2014, in Ground-based and Airborne Instrumentation for Astronomy V. p. 91470L (arXiv:1412.0843), doi:10.1117/12.2055132
Davis O., Devriendt J., Colombi S., Silk J., Pichon C., 2011, MNRAS, 413, 2087
Di Cintio A., Brook C. B., Macciò A. V., Stinson G. S., Knebe A., Dutton A. A., Wadsley J., 2014, MNRAS, 437, 415
Diez-Tejedor A., Gonzalez-Morales A. X., Profumo S., 2014, Phys. Rev. D, 90, 043517
Du X., Behrens C., Niemeyer J. C., 2017, MNRAS, 465, 941

Dunkley J., Bucher M., Ferreira P. G., Moodley K., Skordis C., 2005, MNRAS, 356, 925

El-Zant A., Shlosman I., Hoffman Y., 2001, ApJ, 560, 636

Errani R., Peñarrubia J., Laporte C. F. P., Gómez F. A., 2017, MNRAS, 465, L59

Foreman-Mackey D., Hogg D. W., Lang D., Goodman J., 2013, PASP, 125, 306

Garzilli A., Boyarsky A., Ruchayskiy O., 2015, preprint, (arXiv:1510.07006)

Gilmore G., Wilkinson M., Kleyna J., Koch A., Evans W., Wyse R. F. G., Grebel E. K., 2007, Nuclear Physics B Proceedings Supplements, 173, 15

Giocoli C., Pieri L., Tormen G., 2008, MNRAS, 387, 689

Governato F., et al., 2012, MNRAS, 422, 1231

Guzmán F. S., Ureña-López L. A., 2006, ApJ, 645, 814

Guzman F. S., Urena-Lopez L. A., 2004, Phys. Rev., D69, 124033

Hložek R., Marsh D. J. E., Grin D., Allison R., Dunkley J., Calabrese E., 2016, preprint, (arXiv:1607.08208)

Hlozek R., Grin D., Marsh D. J. E., Ferreira P. G., 2015, Phys. Rev. D, 91, 103512

Hu W., Barkana R., Gruzinov A., 2000, Physical Review Letters, 85, 1158

Hui L., Ostriker J. P., Tremaine S., Witten E., 2017, Phys. Rev. D, 95, 043541

Iršič V., Viel M., Haehnelt M. G., Bolton J. S., Becker G. D., 2017, preprint, (arXiv:1703.04683)

Jardel J. R., Gebhardt K., 2013, preprint, (arXiv:1309.2637)

Jardel J., Gebhardt K., Fabricius M., Drory N., 2012, in American Astronomical Society Meeting Abstracts #219. p. 244.20

Jones E., Oliphant T., Peterson P., et al., 2001–, SciPy: Open source scientific tools for Python, http://www.scipy.org/

Kaplinghat M., Tulin S., Yu H.-B., 2016, Physical Review Letters, 116, 041302

Khlopov M., Malomed B., Zeldovich I., 1985, MNRAS, 215, 575

Kleyna J. T., Wilkinson M. I., Evans N. W., Gilmore G., 2001, ApJ, 563, L115

Kleyna J., Wilkinson M. I., Evans N. W., Gilmore G., Frayn C., 2002, MNRAS, 330, 792

Lewis A., Challinor A., Lasenby A., 2000, ApJ, 538, 473

Łokas E. L., 2009, MNRAS, 394, L102

Long R. J., Mao S., 2010, MNRAS, 405, 301

Lora V., Magaña J., Bernal A., Sánchez-Salcedo F. J., Grebel E. K., 2012, J. Cosmology Astropart. Phys., 2, 11

Lovell M. R., Frenk C. S., Eke V. R., Jenkins A., Gao L., Theuns T., 2014, MNRAS, 439, 300

Marsh D. J. E., 2016, Phys. Rep., 643, 1

Marsh D. J. E., Ferreira P. G., 2010, Phys. Rev. D, 82, 103528

Marsh D. J. E., Pop A.-R., 2015, MNRAS, 451, 2479

Marsh D. J. E., Silk J., 2014, MNRAS, 437, 2652

Mateo M. L., 1998, ARA&A, 36, 435

Mateo M., Olszewski E. W., Walker M. G., 2008, ApJ, 675, 201

Matos T., Urena-Lopez L. A., 2000, Class. Quant. Grav., 17, L75

Matos T., Urena-Lopez L. A., 2001, Phys. Rev., D63, 063506

McConnachie A. W., 2012, AJ, 144, 4

Mocz P., Vogelsberger M., Robles V., Zavala J., Boylan-Kolchin M., Hernquist L., 2017

Murgia R., Merle A., Viel M., Totzauer M., Schneider A., 2017, preprint, (arXiv:1704.07838)

Navarro J. F., Eke V. R., Frenk C. S., 1996, MNRAS, 283, L72

Navarro J. F., Frenk C. S., White S. D. M., 1997, ApJ, 490, 493

Nipoti C., Binney J., 2015, MNRAS, 446, 1820

Paredes A., Michinel H., 2016, Physics of the Dark Universe, 12, 50

Peñarrubia J., Pontzen A., Walker M. G., Koposov S. E., 2012, ApJ, 759, L42

Planck Collaboration et al., 2014, A&A, 571, A16

Planck Collaboration et al., 2016, preprint, (arXiv:1605.02985)

Pontzen A., Governato F., 2014, Nature, 506, 171

Press W. H., Ryden B. S., Spergel D. N., 1990, Physical Review Letters, 64, 1084

Read J. I., Gilmore G., 2005, MNRAS, 356, 107

Read J. I., Agertz O., Collins M. L. M., 2016, MNRAS, 459, 2573

Richardson T., Fairbairn M., 2014, MNRAS, 441, 1584

Ruffini R., Bonazzola S., 1969, Phys. Rev., 187, 1767

Sahni V., Wang L.-M., 2000, Phys. Rev., D62, 103517

Salucci P., Wilkinson M. I., Walker M. G., Gilmore G. F., Grebel E. K., Koch A., Martins C. F., Wyse R. F. G., 2012, Mon. Not. Roy. Astron. Soc., 420, 2034

Sarkar A., Mondal R., Das S., Sethi S. K., Bharadwaj S., Marsh D. J. E., 2016, J. Cosmology Astropart. Phys., 4, 012

Sawala T., Scannapieco C., Maio U., White S., 2010, MNRAS, 402, 1599

Sawala T., et al., 2016, MNRAS, 457, 1931

Schive H.-Y., Chiueh T., Broadhurst T., 2014a, Nature Physics, 10, 496

Schive H.-Y., Liao M.-H., Woo T.-P., Wong S.-K., Chiueh T., Broadhurst T., Hwang W.-Y. P., 2014b, Phys. Rev. Lett., 113, 261302

Schive H.-Y., Chiueh T., Broadhurst T., Huang K.-W., 2016, ApJ, 818, 89

Schneider A., 2016, J. Cosmology Astropart. Phys., 4, 059

Schwabe B., Niemeyer J. C., Engels J. F., 2016, Phys. Rev. D, 94, 043513

Seidel E., Suen W. M., 1991, Phys. Rev. Lett., 66, 1659

Sheth R. K., Tormen G., 1999, MNRAS, 308, 119

Sin S.-J., 1994, Phys. Rev., D50, 3650

Spergel D. N., Steinhardt P. J., 2000, Physical Review Letters, 84, 3760

Spergel D. N., Flauger R., Hložek R., 2015, Phys. Rev. D, 91, 023518

Strigari L. E., Bullock J. S., Kaplinghat M., 2007, ApJ, 657, L1

Strigari L. E., Frenk C. S., White S. D. M., 2010, MNRAS, 408, 2364

Suárez A., Robles V. H., Matos T., 2014, Astrophysics and Space Science Proceedings, 38, 107

Tremaine S., Gunn J. E., 1979, Phys. Rev. Lett., 42, 407

Tulin S., Yu H.-B., Zurek K. M., 2013, Phys. Rev. D, 87, 115007

Uhlemann C., Kopp M., Haugg T., 2014, Phys. Rev. D, 90, 023517

Ureña-López L. A., Gonzalez-Morales A. X., 2016, J. Cosmology Astropart. Phys., 7, 048

Urena-Lopez L. A., 2002, Class. Quant. Grav., 19, 2617

Urena-Lopez L. A., Robles V. H., Matos T., 2017

Veltmaat J., Niemeyer J. C., 2016a, preprint, (arXiv:1608.00802)

Veltmaat J., Niemeyer J. C., 2016b, Phys. Rev. D, 94, 123523

Vogelsberger M., Zavala J., Loeb A., 2012, MNRAS, 423, 3740

Vogelsberger M., Zavala J., Cyr-Racine F.-Y., Pfrommer C., Bringmann T., Sigurdson K., 2016, MNRAS, 460, 1399

Walker M., 2013, Dark Matter in the Galactic Dwarf Spheroidal Satellites. Springer Science+Business Media Dordrecht, p. 1039, doi:10.1007/978-94-007-5612-0˙20

Walker M. G., Peñarrubia J., 2011, ApJ, 742, 20

Walker M. G., Mateo M., Olszewski E. W., Gnedin O. Y., Wang X., Sen B., Woodroofe M., 2007, Astrophys. J., 667, L53

Walker M. G., Mateo M., Olszewski E. W., 2009a, AJ, 137, 3100

Walker M. G., Mateo M., Olszewski E. W., Peñarrubia J., Wyn Evans N., Gilmore G., 2009b, ApJ, 704, 1274

Walker M. G., Mateo M., Olszewski E. W., Peñarrubia J., Wyn Evans N., Gilmore G., 2010, ApJ, 710, 886

Weinberg D. H., Bullock J. S., Governato F., Kuzio de Naray R., Peter A. H. G., 2015, Proceedings of the National Academy of Science, 112, 12249

Widrow L. M., Kaiser N., 1993, ApJ, 416, L71

Wilkinson M. I., Kleyna J., Evans N. W., Gilmore G., 2002, MNRAS, 330, 778

Wolf J., Martinez G. D., Bullock J. S., Kaplinghat M., Geha M.,

Muñoz R. R., Simon J. D., Avedo F. F., 2010, MNRAS, 406, 1220

Zhu Q., Marinacci F., Maji M., Li Y., Springel V., Hernquist L., 2016, MNRAS, 458, 1559

de Jong R. S., et al., 2012, in Ground-based and Airborne Instrumentation for Astronomy IV. p. 84460T (arXiv:1206.6885), doi:10.1117/12.926239

APPENDIX A: JEANS ANALYSIS

Following the standard parametric analysis analysis (Walker et al. 2009b; Salucci et al. 2012) we will consider that the stellar component in each individual galaxy is in dynamical equilibrium and that stars are kinematic tracers of the underlying DM potential . Assuming, further, spherical symmetry, Jeans's equation relates the mass profile of the DM halo,

$$M(r) = 4\pi \int_0^r \rho(r') r'^2 dr' \qquad (A1)$$

to the first moment of the stellar distribution function,

$$\frac{1}{\nu} \frac{d}{dr} \left(\nu \langle v_r^2 \rangle \right) + 2 \frac{\beta \langle v_r^2 \rangle}{r} = -\frac{GM}{r^2} . \qquad (A2)$$

Above, $\nu(r)$, $\langle v_r^2(r) \rangle$, and $\beta(r) = 1 - \langle v_\theta^2 \rangle / \langle v_r^2 \rangle$ are the three-dimensional density, radial velocity dispersion, and orbital anisotropy, respectively, of the stellar component. The parameter β quantifies the degree of radial stellar anisotropy: if all orbits are circular $\langle v_r^2 \rangle = 0$, and then $\beta = \infty$; if the orbits are isotropic $\langle v_r^2 \rangle = \langle v_\theta^2 \rangle$, and $\beta = 0$; finally, if all orbits are perfectly radial, $\langle v_\theta^2 \rangle = 0$, then $\beta = 1$. There is no preference *a priori* for either radially, $\beta > 0$, or tangentially, $\beta < 0$, biased systems.

The function F depending on the anisotropy is given by:

$$F(\beta, R, r') \equiv \int_R^{r'} dr \left(1 - \beta \frac{R^2}{r^2} \right) \frac{r^{-2\beta+1}}{\sqrt{r^2 - R^2}} , \qquad (A3)$$

For the stellar density we adopted a Plummer profile,

$$I(R) = \frac{L}{\pi R_{\text{half}}^2} \frac{1}{[1 + (R/R_{\text{half}})^2]^2} , \qquad (A4)$$

where L is the total luminosity of the object and R_{half}, the half-light radius. The values of these two quantities for each of the eight classical dSphs are listed in Table I of (Walker et al. 2009b). Under the assumption of spherical symmetry the corresponding three-dimensional stellar density associated with the Plummer profile takes the form

$$\nu(r) = \frac{3L}{4\pi r_{\text{half}}^3} \frac{1}{[1 + (r/r_{\text{half}})^2]^{5/2}} . \qquad (A5)$$

For the Jeans analysis we adopted the following priors:

$$-3.0 < \quad \log 10 \left(\frac{m_a}{10^{-22} \text{eV}} \right) \quad < 5.0 , \quad (A6a)$$

$$-3.0 < \quad \log 10 \left(\frac{\rho_{\text{sol,i}}}{2.42 \times 10^9 M_\odot \text{kpc}^{-3}} \right) \quad < 3.0 , \quad (A6b)$$

$$-5 < \quad \ln (\epsilon_i) \quad < 0 , \quad (A6c)$$

$$-3 < \quad \ln \left(\frac{r_{s,i}}{\text{kpc}} \right) \quad < 3 , \quad (A6d)$$

$$-3 < \quad -\ln (1 - \beta_i) \quad < 5. . \quad (A6e)$$

APPENDIX B: TRIANGLE PLOTS OF MOCK GALAXIES

Here we present the triangle plots from the statistical analysis of the mock data presented in Sec. 4.1 generated as isotropic, $\beta = 0$, Fig.B1, and with an Osipkov-Merrit anisotropy profile Fig.B2. In both cases the analysis was done with the two estimators: M-estimator (green line) and $\langle \sigma_{\text{los}}^2 \rangle$-fit (blue lines). We can see that for all the mocks the $\langle \sigma_{\text{los}}^2 \rangle$-fit recovers very well the true values of the axion mass and the central density. These fits included the parameters corresponding to the external NFW part of the profile, however they are not shown as they are fully unconstrained.

APPENDIX C: CMB OPTICAL DEPTH CONSTRAINTS

On of the constraints that can be set by the epoch of reionization is given by the CMB Thompson scattering optical depth, τ, which is an integral over the reionization history to redshift z, given by:

$$\tau(z) = \int_0^z \frac{c(1+z')^2}{H(z')} Q_{HII}(z') \sigma_T \bar{n}_H (1 + \eta Y/4X) dz', \quad (C1)$$

where the function $Q_{II}(z)$, volume-filling fraction of ionized hydrogen, and the mean comoving hydrogen number $\bar{n}_H$, encodes the reionization history. Here, c is the speed of light, $H(z)$ is the Hubble parameter, σ_T is the Thompson scattering cross section, and η corresponds to the state of the the Helium. The optical depth depend, in general, on the properties of the assumed DM model, mainly through the shape of the linear mass power spectrum. See (Bozek et al. 2015) for a detailed computation of the optical depth in the axion Dark Matter Framework.

Constraints on the CMB Thompson scattering optical depth offers an interesting window onto ULAs in dSphs, as demonstrated in Fig. C1. In this figure we collate the results of (Bozek et al. 2015) for τ based on concordance reionization models for ULAs, with error bands representing the modeling uncertainty. We compare these results to two different values for τ determined from CMB temperature and polarization power spectrum measurements. The combination of *Planck* temperature power spectrum and WMAP low-ℓ polarization (Planck Collaboration et al. 2014; Bennett et al. 2013, "Planck+WP"), gives $\tau = 0.089 \pm 0.012$ (the revision of Spergel et al. 2015, to $\tau = 0.09 \pm 0.13$ does not affect our conclusions). On the other hand, the recent *Planck* low-ℓ polarization results using the HFI τ posterior gives a much lower and tighter value of $\tau = 0.055 \pm 0.009$ (Planck Collaboration et al. 2016, "Planck HFI"). The limit on ULA mass from our reanalysis of the dSph data, $m_{22} < 0.4$, is in considerable tension with the Planck+WP τ constraints, yet is consistent with the Planck HFI constraint. This demonstrates the power that future constraints on the epoch of reionization from CMB polarization will have to probe the nature of DM (e.g. Calabrese et al. 2014), and the importance of understanding possible low-ℓ polarization systematic errors that could be causing a tension between *Planck* and WMAP τ measurements.
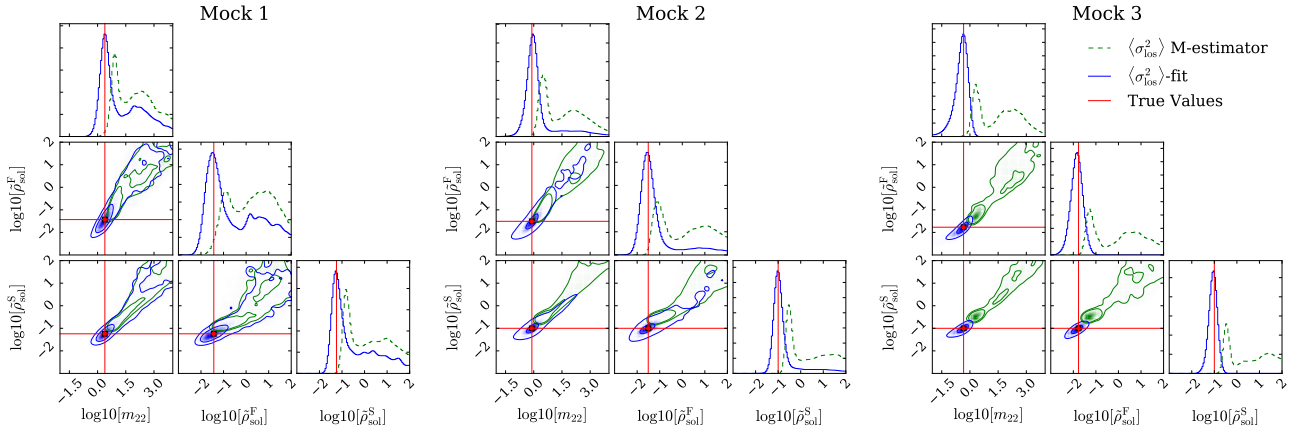
Figure B1. Full analysis of three sets of mocks already presented in Fig 7, but only for the particular case of $\beta = 0$. Green contours, dashed lines, use the constant virial factor M-estimator, Eq. (2) with $\mu = 2/5$, and blue contours use the $\langle \sigma_{\mathrm{los}}^2 \rangle$-fit, Eq. (3). As explained before, both estimators recover central axion mass values close to the input (red line), and some bimodality can be clearly seen when the prior mass range is large. The M-estimator has a bias to larger axion masses, while the $\langle \sigma_{\mathrm{los}}^2 \rangle$-fit recovers an unbiased value. Contours indicate the 1 and 2-σ confidence levels. axion mass and soliton density are given in units 10^{-22}eV and $2.42 \times 10^9 M_\odot \mathrm{kpc}^{-3}$ respectively.
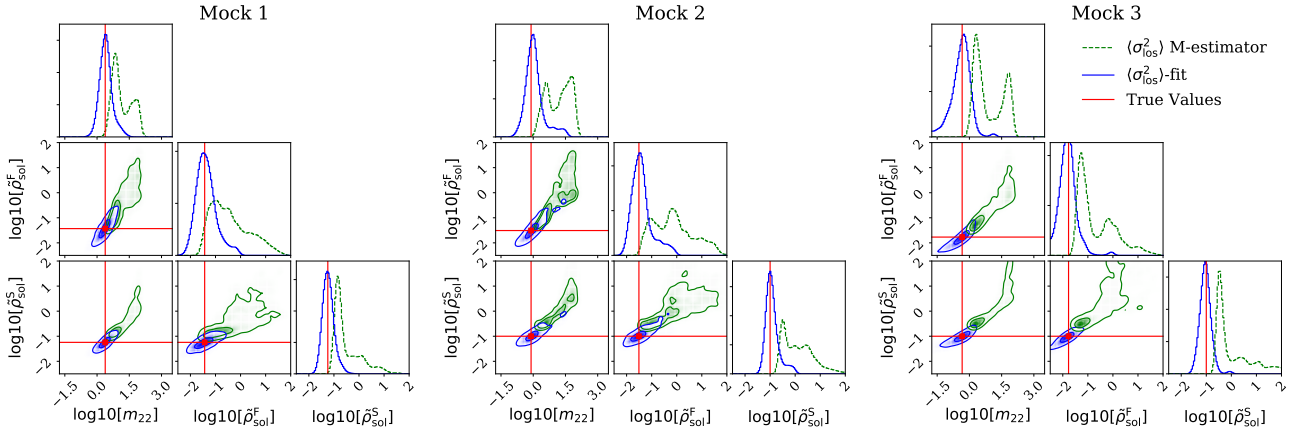
Figure B2. Same as Fig. B1 but for the set of mocks constructed with an Osipkov-Merrit anisotropy profile. Again, the M-estimator has a bias to larger axion masses, while the $\langle \sigma_{\mathrm{los}}^2 \rangle$-Fit recovers anunbiased value. Contours indicate the 1 and 2-σ confidence levels. axion mass and soliton density are given in units 10^{-22}eV and $2.42 \times 10^9 M_\odot \mathrm{kpc}^{-3}$ respectively.
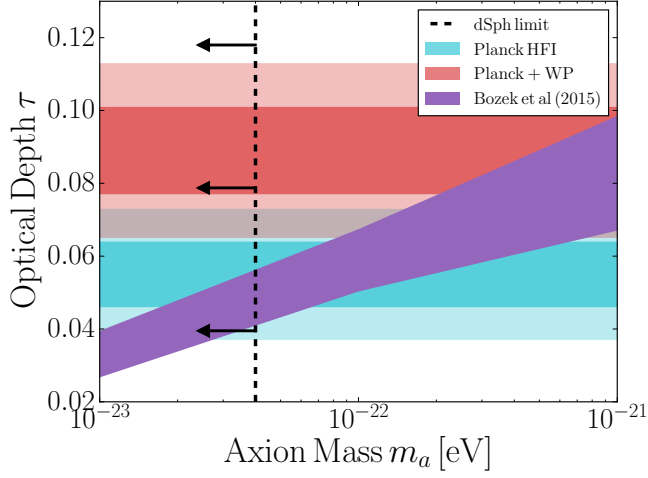
Figure C1. The optical depth to reionization, τ, computed in concordance models for ULAs, where the error band represents systematic modelling uncertainty (Bozek et al. 2015). The horizontal bands represent 1 and 2-σ constraints on τ from different CMB polarization power spectrum measurements. The axion mass limit from dSphs produces a reionization history consistent with the recent Planck HFI results, but in considerable tension with earlier results from Planck+WP.